ELSEVIER

Journal of Nuclear Materials 279 (2000) 273–285

journal of nuclear materials

www.elsevier.nl/locate/jnucmat

Simulation of hydrogen embrittlement in zirconium alloys under stress and temperature gradients

A.G. Varias [a,*], A.R. Massih [b,c]

[a] *Solid Mechanics Research Office, Makedonias 17, N. Iraklio, 14121 Athens, Greece*
[b] *ABB Atom AB, S-721 63, Västerås, Sweden*
[c] *Luleå University of Technology, S-971 87, Luleå, Sweden*

Received 19 May 1999; accepted 7 December 1999

Abstract

A finite element model is presented for hydrogen embrittlement of zirconium alloys. The model takes into account the coupled processes of hydrogen diffusion, non-mechanical energy flow, hydride precipitation, hydride/solid solution deformation and fracture.The model has been tested successfully against the Sawatzky experiment and exact analytical solutions on hydrogen diffusion and hydride precipitation under a temperature gradient. Based on this model, the hydrogen embrittlement of a Zircaloy-2 cracked plate, is studied under tensile stress and temperature gradient. The initial and boundary conditions are according to those encountered in the fuel cladding of light water reactors during operation. The strong effect of crack tip stress intensification on hydrogen diffusion and initial hydride precipitation is shown. The problem is also studied by considering near-tip material damage which affects hydride precipitation significantly. © 2000 Elsevier Science B.V. All rights reserved.

PACS: 46.50.+a; 81.40.Np; 81.05.Je; 02.70.Dh

1. Introduction

Zirconium alloys are the major structural materials within the fuel region of light water reactors. They are invariably used as fuel cladding, fuel channels and often as fuel assembly spacer grids. During reactor operation, zirconium alloys pick up part of the hydrogen, which is released from the oxidation process of zirconium by water. Hydrogen in solid solution diffuses under the presence of concentration, temperature, and stress gradients. For example, hydrogen diffuses towards the colder regions under a thermal gradient or it diffuses towards the higher hydrostatic stress regions under a stress gradient [1].

Hydrogen in zirconium alloys has a low solubility which leads to formation of zirconium hydrides. These hydrides are brittle and degrade the mechanical properties of zirconium alloys [2]. These changes in mechanical properties need to be considered in component design-life evaluation. Hence, understanding of hydrogen behavior becomes important as fuel burnups are increased which results in increased corrosion and hydrogen pickup [3].

The phenomena of hydrogen diffusion and hydrogen redistribution in zirconium alloys have been studied both experimentally and theoretically in the past decades. Sawatsky [4] and Markowitz [5] made early experimental investigations on thermal diffusion and redistribution of hydrogen in Zircaloy-2 under temperature gradient. Later Asher and Trowse [6] provided a descriptive explanation of hydrogen redistribution in Zircaloy-2 cladding tubes subjected to temperature gradient while corroding. More recently an analytical model [7] was developed to explain and predict the hydride distribution observed in fuel cladding of boiling water reactors, under the presence of axial and radial temperature gradients. Also Kammenzind et al. [8] have studied experimentally the hydrogen pickup and redistribution in alpha-annealed Zircaloy-4 in a test reactor

---

[*] Corresponding author. Tel.: +30-1 28 49 916; fax: +30-1 28 49 916.
E-mail address: varias@hol.gr (A.G. Varias).

PII: S0022-3115(99)00286-X

as well as by performing ex-reactor tests; these results were evaluated by a phenomenological diffusion model.

The stress-induced movement of hydrogen in zirconium alloys in the presence of hydrides was investigated by Ells and Simpson [9]. They estimated the reorientation of hydride which occurs from stress-induced growth of hydride. Maki and Sato [10] also studied the effect of hydride platelets on thermal diffusion of hydrogen in recrystallized Zircaloy-2. They introduced a stress gradient term in the diffusion equation. They also approximated the stress effect on hydrogen terminal solid solubility. Their calculations of the radial hydrogen distribution in a cladding tube, subjected to a temperature difference across the wall, described the experimental results very well.

The mechanism of hydrogen embrittlement includes (i) hydrogen diffusion, (ii) energy flow and (iii) formation of brittle hydrides. All three phenomena are coupled. Thus, the simulation of damage growth in zirconium alloy fuel cladding, caused by hydrogen embrittlement, requires the simultaneous solution of hydrogen diffusion, energy flow, material deformation and fracture. The numerical procedure, presented in this study, takes into account hydride formation and extends previous studies on coupled hydrogen diffusion and material deformation [11], in order to incorporate hydrogen thermal diffusion [12] and energy flow. Consequently, the present model can take into account important temperature gradient effects on hydrogen redistribution [7]. Initial damage growth is also considered by using the de-cohesion model for fracture (e.g. [13–15]).

The primary objective of the paper is the presentation of a hydrogen embrittlement model, which takes into account the coupling of the above mentioned physical processes. Based on this model, the strong effects of crack tip stress intensification and material damage on hydrogen diffusion and initial hydride precipitation are shown. The physical mechanism of delayed hydride cracking, observed in zirconium alloys can be also simulated by using the present model [16]. However, this simulation is beyond the scope of the present introductory study and it will be discussed in a separate paper.

The structure of the paper is as follows. In Section 2, the equations governing hydrogen diffusion, hydride formation, energy flow and material deformation and fracture are presented. In Section 3 the finite element implementation of the governing equations is briefly discussed. Section 4 presents the numerical simulation of Sawatzky's hydrogen thermal diffusion experiments [4], in order to test the accuracy of the numerical model; when hydrogen is in solid solution, the finite element results are compared with analytical expressions in Appendix A. The simulation of hydrogen embrittlement in a cracked plate, under tensile stress and temperature gradient is presented in Sections 5 and 6. The initial and boundary conditions approach those encountered in nuclear fuel cladding, during reactor operation. Finally, concluding remarks are given in Section 7.

In the present study Zircaloy-2 and δ-hydride ($ZrH_{1.66}$) are considered. All material properties, required for the simulation, are given in Table 1.

Table 1
Material properties, used in finite element calculations, which correspond to Zircaloy-2 and δ-hydride ($ZrH_{1.66}$). The source of the information is included

E, ν	80.4 GPa, 0.369	Ref. [27]
E_i, E_f	80.4 GPa, 80.4 GPa	Assumption
$\sigma_{\mathrm{Zr}}, \sigma_{\mathrm{hr}}$	1740 MPa, 580 MPa	Ref. [27], (σ_{Zr} is assumed to be equal to 3×(irradiated material yield stress))
$K_{\mathrm{I}}^{\mathrm{Zr}}$	$30 + 0.045(T - 300)\ \mathrm{MPa}\sqrt{\mathrm{m}}$	Ref. [38]
$K_{\mathrm{I}}^{\mathrm{hr}}$	$3.22 + 0.02205(T - 300)\ \mathrm{MPa}\sqrt{\mathrm{m}}$	Ref. [27]
δ_0	2 μm	Assumption
D^{H}	$2.17 \times 10^{-7} \exp(-35087.06/RT)\ \mathrm{m^2/s}$	Ref. [4]
Q^{H}	25122 J/mol	Ref. [4]
C^{TS}	$6.3741 \times 10^{5} \exp(-34542.75/RT)\ \mathrm{mol/m^3}$	Ref. [39], (experimental data which include hydride accommodation strain energy)
$C^{\mathrm{H,hr}}$	$1.02 \times 10^{5}\ \mathrm{mol/m^3}$	Calculation
$\bar{V}^{\mathrm{H}}, \bar{V}^{\mathrm{Zr}}, \bar{V}^{\mathrm{hr}}$	$7 \times 10^{-7}, 14.06 \times 10^{-6}, 16.3 \times 10^{-6}\ \mathrm{m^3/mol}$	Ref. [40] for $\overline{V}^{\mathrm{H}}$, [41] for $\overline{V}^{\mathrm{hr}}$, $\bar{V}^{\mathrm{Zr}}$ was calculated
$\theta^{\mathrm{hr}}, \theta^{\mathrm{H}}$	0.1636, 0.1	Ref. [41] for θ^{hr}, assumption for θ^{H}
x	1.66	δ-hydride (ZrH_x) (e.g. [21])
ρ	$6490\ \mathrm{kg/m^3}$	Pure zirconium density
$\Delta\overline{H}^{\mathrm{hr}}$	−63517.41 J/mol	Calculation, based on the experimental terminal solid solubility of hydrogen
k	$9.37683 + 0.0118T$ W / m K	Ref. [42]
c_p	$226.69 + 0.206639T - 6.4925 \times 10^{-5}T^2$ J/K kg	Ref. [42]
a	$5.96 \times 10^{-6}\mathrm{K}^{-1}$	Average value, based on [42]

2. Governing equations

2.1. Thermodynamic equations of motion

Energy flow and diffusion of mass are generally coupled processes. A detailed discussion and relevant references for the thermodynamic treatment of energy-flow/diffusion as well as of other coupled phenomena are presented by Denbigh [12].

According to the empirical laws of irreversible processes, under a wide range of experimental conditions, the irreversible flows are linear functions of thermodynamic forces. For example, Fourier's law for heat conduction expresses that the components of the heat flow are linear functions of the components of temperature gradient, and Fick's law establishes a linear relation between the diffusion flow of matter and the concentration gradient. Also included in these descriptions are laws of cross-phenomena such as thermal diffusion, in which the diffusion flow depends linearly on both the concentration and temperature gradients. Near equilibrium the currents, J_i, are approximated by the linear relations:

$$J_i^{\mathrm{E}} = L^{\mathrm{E}} X_i^{\mathrm{E}} + L^{\mathrm{EH}} X_i^{\mathrm{H}}, \tag{1}$$

$$J_i^{\mathrm{H}} = L^{\mathrm{HE}} X_i^{\mathrm{E}} + L^{\mathrm{H}} X_i^{\mathrm{H}}, \tag{2}$$

where J_i^{E} and J_i^{H} are the non-mechanical energy flux and the hydrogen flux, respectively. The quantities L^{E}, L^{H}, L^{EH} and L^{HE} are phenomenological coefficients. Note that $L^{\mathrm{EH}} = L^{\mathrm{HE}}$ due to Onsager reciprocity relation [12]. X_i^{E} and X_i^{H} denote the thermodynamic forces driving energy flow and hydrogen diffusion, respectively. They are given by the following relations:

$$X_i^{\mathrm{E}} = -\frac{1}{T}\frac{\partial T}{\partial x_i}, \tag{3}$$

$$X_i^{\mathrm{H}} = -T\frac{\partial}{\partial x_i}\left(\frac{\mu^{\mathrm{H}}}{T}\right). \tag{4}$$

T is the absolute temperature and μ^{H} the chemical potential of hydrogen in solid solution. It can be shown that, according to relations (3) and (4), the rate of internal generation of entropy per unit volume equals to $(J_i^{\mathrm{E}} X_i^{\mathrm{E}} + J_i^{\mathrm{H}} X_i^{\mathrm{H}})/T$. It is noted that the energy flux includes conducted heat, which is described by Fourier's law, and the energy transported by the diffusing hydrogen.

2.2. Hydrogen diffusion

Under temperature and chemical potential gradients, the hydrogen flux in a zirconium alloy satisfies the following relation:

$$J_k^{\mathrm{H}} = -(1-f)\frac{D^{\mathrm{H}} C^{\mathrm{H}}}{RT}\left(\frac{\partial \mu^{\mathrm{H}}}{\partial x_k} + \frac{Q^{\mathrm{H}}}{T}\frac{\partial T}{\partial x_k}\right), \tag{5}$$

where R is the gas constant ($=8.314$ J/K mol), f the hydride volume fraction and C^{H}, D^{H} and Q^{H} are the concentration, the diffusion coefficient and the heat of transport of hydrogen in solid solution, respectively. Relation (5) is derived by considering the relation for hydrogen flux in the solid solution (e.g. [1,4]) and neglecting hydrogen diffusion in the hydride, which is relatively very slow.

Conservation of hydrogen mass for an arbitrary volume and divergence theorem leads to the differential equation, which governs hydrogen diffusion:

$$\frac{\mathrm{d}C^{\mathrm{HT}}}{\mathrm{d}t} = -\frac{\partial J_k^{\mathrm{H}}}{\partial x_k}. \tag{6}$$

Note that the total hydrogen concentration, C^{HT}, is related to the concentration of hydrogen in solid solution, C^{H}, and the hydride concentration, $C^{\mathrm{H,hr}}$, as follows:

$$C^{\mathrm{HT}} = fC^{\mathrm{H,hr}} + (1-f)C^{\mathrm{H}}, \tag{7}$$

where C^{H} is defined with respect to the volume occupied by the solid solution, i.e. $(1-f)V$. C^{H} is equal to the hydrogen terminal solid solubility, C^{TS}, when $f \neq 0$. Similarly $C^{\mathrm{H,hr}}$ is defined with respect to the volume occupied by the hydride, i.e. fV, and therefore it can be considered constant, independent of temperature.

2.3. Non-mechanical energy flow

By employing relation (5) for hydrogen flux as well as the flow equations of irreversible thermodynamics (1–2), one may derive the relation for non-mechanical energy flux [17]

$$J_i^{\mathrm{E}} = (Q^{\mathrm{H}} + \mu^{\mathrm{H}})J_i^{\mathrm{H}} - k\frac{\partial T}{\partial x_i}. \tag{8}$$

k is the thermal conductivity of zirconium alloy which has been taken equal to the thermal conductivity of the hydride. Note that in (8) the first term of the right-hand side is related to the energy transported by hydrogen atoms, while the second term is the conducted heat, governed by the empirical law of Fourier.

The governing equation for energy flow is derived, by considering the differential equation for the conservation of energy

$$\rho\frac{\mathrm{d}u}{\mathrm{d}t} = \sigma_{ij}\frac{\mathrm{d}\varepsilon_{ij}}{dt} - \frac{\partial J_k^{\mathrm{E}}}{\partial x_k}, \tag{9}$$

where ρ, u, σ_{ij} and ε_{ij} are material's density, internal energy per unit mass, stress and strain tensors, respectively, as well as by considering continuum thermodynamics based on a caloric equation of state (e.g. [18]).

Then, for a particle of the continuum, the internal energy variation satisfies the following relation:

$$\rho \frac{\mathrm{d}u}{\mathrm{d}t} = \rho T \frac{\mathrm{d}s}{\mathrm{d}t} + \sigma_{ij} \frac{\mathrm{d}\varepsilon_{ij}}{\mathrm{d}t} + \mu^{\mathrm{H}} \frac{\mathrm{d}C^{\mathrm{HT}}}{\mathrm{d}t}, \tag{10}$$

where s is the specific entropy. Relation (10) is derived in [17] by assuming that hydride precipitation occurs under equilibrium conditions

$$\mu^{\mathrm{hr}} = \mu^{\mathrm{Zr}} + x\mu^{\mathrm{H}}, \tag{11}$$

where μ^{Zr} is the chemical potential of zirconium and μ^{hr} is the chemical potential of the hydride (ZrH_x). By manipulating (6), (9) and (10) the governing equation for energy flow is derived [17]

$$\rho c_p \frac{\mathrm{d}T}{\mathrm{d}t} + \frac{\Delta \overline{H}^{\mathrm{hr}}}{\overline{V}^{\mathrm{hr}}} \frac{\mathrm{d}f}{\mathrm{d}t} = \frac{\partial}{\partial x_i}\left(k \frac{\partial T}{\partial x_i}\right) - J_n^{\mathrm{H}} \frac{\partial \mu^{\mathrm{H}}}{\partial x_n}, \tag{12}$$

where c_p is the specific heat of Zr-alloy at constant pressure, which is assumed to be equal to the specific heat of the alloy under constant stress, $\Delta \overline{H}^{\mathrm{hr}}$ is the enthalpy associated with the formation of a mole of hydride and $\overline{V}^{\mathrm{hr}}$ is the molal hydride volume.

2.4. Hydrogen chemical potential and terminal solid solubility in Zirconium under stress

According to the discussion in Sections 2.1 to 2.3, the simulation of hydrogen diffusion and energy flow requires the knowledge of the hydrogen chemical potential and terminal solid solubility. Both quantities depend on applied stress. The derivation, which is presented in detail in [17], is based on the study by Li et al. [19].

If it is assumed that the hydrogen dissolution has no effect on the elastic moduli of zirconium alloy, the chemical potential of hydrogen, being in solid solution in zirconium alloy under stress, is given by the following relation:

$$\mu^{\mathrm{H}} = \mu^{\mathrm{H},0} + \overline{V}^{\mathrm{H}} \left(\tfrac{1}{2} M_{ijkl} \sigma_{ij} \sigma_{kl} - \tfrac{1}{3} \sigma_{mm} \right), \tag{13}$$

where $\mu^{\mathrm{H},0}$ is the hydrogen chemical potential under stress-free conditions, $\overline{V}^{\mathrm{H}}$ is the molal hydrogen volume in solid solution and M_{ijkl} is the elastic compliance tensor of zirconium alloy. The first term in parenthesis can be neglected for being relatively small. Then a relation is derived, which is more often used in literature. When an ideal solution is considered, the stress-free chemical potential is well-known:

$$\mu^{\mathrm{H},0} = \mu^{\mathrm{H,RS}} + RT \ln \left(C^{\mathrm{H}} \overline{V} \right), \tag{14}$$

where $\mu^{\mathrm{H,RS}}$ is the chemical potential of hydrogen in a 'standard' (i.e. reference) state and $\overline{V}$ is the molal volume of solid solution.

Hydride precipitation occurs when the concentration of hydrogen in the solid solution exceeds the terminal solid solubility. Due to the expansion of the hydride, during formation, as well as due to the effect of stress on hydrogen chemical potential, the terminal solid solubility depends also on the applied stress

$$C^{\mathrm{TS}} = C^{\mathrm{TS},0} \exp\left(\frac{\overline{w}_{\mathrm{acc}} + \overline{w}_{\mathrm{int}}}{xRT} \right) \exp\left[\frac{\overline{V}^{\mathrm{H}}}{RT} \left(\frac{\sigma_{mm}}{3} - \frac{1}{2} M_{ijkl} \sigma_{ij} \sigma_{kl} \right) \right], \tag{15}$$

where $C^{\mathrm{TS},0}$ is the hydrogen terminal solid solubility under stress free conditions; $\overline{w}_{\mathrm{acc}}$ and $\overline{w}_{\mathrm{int}}$ are the strain energy of accommodation and the interaction strain energy per mole of hydride, respectively. They are given by [20]

$$\overline{w}_{\mathrm{acc}} = -\tfrac{1}{2} \int_{\overline{V}^{\mathrm{hr}}} \sigma_{ij}^{\mathrm{I}} \varepsilon_{ij}^{\mathrm{T}} \, \mathrm{d}V, \tag{16}$$

$$\overline{w}_{\mathrm{int}} = - \int_{\overline{V}^{\mathrm{hr}}} \sigma_{ij} \varepsilon_{ij}^{\mathrm{T}} \, \mathrm{d}V. \tag{17}$$

The hydride transformation strain, $\varepsilon_{ij}^{\mathrm{T}}$, under no external loading leads to the development of compressive stresses in the hydride, σ_{ij}^{I}. Transformation strain is assumed to be isotropic in the present study. A simplified version of relation (15) which does not include the elastic compliance term has been presented by Puls [21]. Note that the experimental studies for the calculation of hydrogen terminal solid solubility in zirconium alloy provide data, which incorporate hydride accommodation effect.

2.5. Solid solution – hydride elastic deformation

In the present mathematical formulation all material phases are taken as elastic. It is also assumed that the elastic properties of hydride and solid solution are identical and do not depend on hydrogen concentration. The same assumption has been made in previous studies on hydride induced embrittlement (e.g. [11,22]).

The material deformation is coupled with hydrogen diffusion and energy flow due to the strains, which are caused by hydrogen dissolution, hydride formation and thermal expansion:

$$\frac{\mathrm{d}\sigma_{ij}}{\mathrm{d}t} = M_{ijkl}^{-1} \left(\frac{\mathrm{d}\varepsilon_{ij}}{\mathrm{d}t} - \frac{\mathrm{d}\varepsilon_{ij}^{\mathrm{H}}}{\mathrm{d}t} - \frac{\mathrm{d}\varepsilon_{ij}^{\mathrm{E}}}{\mathrm{d}t} \right), \tag{18}$$

$$M_{ijkl}^{-1} = \lambda \delta_{ij} \delta_{kl} + \mu \left(\delta_{ik} \delta_{jl} + \delta_{il} \delta_{jk} \right), \tag{19}$$

$$\frac{\mathrm{d}\varepsilon_{ij}^{\mathrm{H}}}{\mathrm{d}t} = \tfrac{1}{3} \delta_{ij} \frac{\mathrm{d}}{\mathrm{d}t} \left[f \theta^{\mathrm{hr}} + (1 - f) C^{\mathrm{H}} \overline{V}^{\mathrm{Zr}} \theta^{\mathrm{H}} \right], \tag{20}$$

$$\frac{\mathrm{d}\varepsilon_{ij}^{\mathrm{E}}}{\mathrm{d}t} = \alpha \delta_{ij} \frac{\mathrm{d}T}{\mathrm{d}t}, \tag{21}$$

where λ, μ are the Lamé constants for Zr-alloy; $\theta^{\mathrm{hr}} = \varepsilon_{kk}^{\mathrm{T}}$ is the hydride expansion, occurring during its precipitation and θ^{H} is the expansion of the zirconium lattice, when a mole of hydrogen corresponds to a mole of zirconium in solid solution. $\overline{V}^{\mathrm{Zr}}$ is the molal volume of zirconium. A relation similar to (20) has been also used in [11]. Finally, α is the thermal expansion coefficient of Zr-alloy.

2.6. De-cohesion model

Ahead of the crack tip there is a fracture process zone, where material deteriorates in a ductile (void growth and coalescence) and/or brittle (hydride cleavage) mode. According to the de-cohesion model, the de-cohesion layer, which is a slice, as thick as the fracture process zone, is taken off the material, along the crack path. Along the boundaries, created by the cut, the cohesive traction is applied. All information on the damage is contained in the distribution of the cohesive traction, which depends on the de-cohesion layer boundary displacements. The shape of the traction-displacement function depends on the failure process. However, in the case of tensile separation, the most important features are the maximum cohesive traction, $\sigma_{\max}$, and the energy of de-cohesion, ϕ_0

$$\phi_0 = \int_0^{\delta_c} \sigma_n \, \mathrm{d}\delta_n, \tag{22}$$

where σ_n is the normal cohesive traction and δ_n is the respective normal displacement which equals the sum of the displacements on both sides of the de-cohesion layer. Also δ_c is the normal displacement, which corresponds to complete failure and consequently to zero normal cohesive traction. Details of the model have been presented in previous publications (e.g. [23,24]). The model has been used for the solution of several fracture problems (e.g. [13–15]).

In the present study, cohesive traction is assumed to vary according to the following relation:

$$\sigma_n = \begin{cases} E_i \frac{\delta_n}{\delta_0}, & \delta_n \leqslant \delta_l, \\ \sigma_{\max}, & \delta_l \leqslant \delta_n \leqslant \delta_f, \\ \sigma_{\max} - E_f \frac{\delta_n - \delta_f}{\delta_0}, & \delta_f \leqslant \delta_n \leqslant \delta_c, \\ 0, & \delta_c \leqslant \delta_n, \end{cases} \tag{23}$$

where δ_0 is a constant length of the order of hydride thickness ($\delta_0 = 2$ μm); E_i and E_f are the de-cohesion moduli, which are assumed to be constant; δ_l is the normal displacement at initiation of damage, at which maximum cohesive traction is reached. Unloading starts, when normal displacement exceeds δ_f. Note that δ_f depends on $\sigma_{\max}$ and ϕ_0 according to the following relation:

$$\delta_f = \left[\phi_0 + \tfrac{1}{2}\sigma_{\max}^2 \delta_0 \left(\frac{1}{E_i} - \frac{1}{E_f}\right)\right] \sigma_{\max}^{-1}. \tag{24}$$

The relations for the energy of de-cohesion and the maximum cohesive traction as well as their derivation, based on experimental measurements, are discussed in the following. As shown by Rice [25], the energy of de-cohesion, related to a cohesive zone ahead of a crack tip, in an elastic material, is equal to the critical value of J-integral, when fracture is imminent:

$$\phi_0 = J_c = \frac{1 - \nu^2}{E} K_{\mathrm{Ic}}^2. \tag{25}$$

J_c and K_{Ic} are the critical values of J-integral and stress intensity factor (e.g. [26]), respectively. Also E and ν are Young's modulus and Poisson's ratio of the material. Consequently, the de-cohesion energy is the energy required per unit crack advance. Ahead of the crack, the material is a composite made of brittle hydride and tough zirconium alloy. Therefore the fracture toughness of the material, expressed by the energy of de-cohesion, depends on hydride volume fraction, f, along the crack plane. A mixture rule has been assumed to describe the energy of de-cohesion of the composite material

$$\phi_0 = f\phi_0^{\mathrm{hr}} + (1 - f)\phi_0^{\mathrm{Zr}}. \tag{26}$$

ϕ_0^{Zr} is the de-cohesion energy of the material, when there is no hydride along the crack plane over a distance from the crack tip $X \gg \delta_0$; i.e. $f = 0$, along the crack plane over the distance X. Therefore, ϕ_0^{Zr} satisfies the following relation:

$$\phi_0^{\mathrm{Zr}} = \frac{(1 - \nu^2)}{E} (K_{\mathrm{I}}^{\mathrm{Zr}})^2, \tag{27}$$

where $K_{\mathrm{I}}^{\mathrm{Zr}}$ is the critical stress intensity factor for zirconium alloy. Table 1 provides values for $K_{\mathrm{I}}^{\mathrm{Zr}}$ as a function of temperature, obtained from experimental data.

In (26), ϕ_0^{hr} is the energy of de-cohesion, when there is only hydride along the crack plane over a distance from the crack tip $X \gg \delta_0$; i.e. $f = 1$, along the crack plane over the distance X. Note that the hydride is surrounded by zirconium alloy. According to previous studies (e.g. [22,27]), the geometry of a long hydride, along the crack plane, corresponds to the threshold stress intensity factor for delayed hydride cracking. Therefore ϕ_0^{hr} is given by the following relation:

$$\phi_0^{hr} = \frac{(1 - \nu^2)}{E} (K_{\mathrm{I}}^{\mathrm{hr}})^2, \tag{28}$$

where $K_{\mathrm{I}}^{\mathrm{hr}}$ is the threshold stress intensity factor for delayed hydride cracking. In Table 1 we provide values for $K_{\mathrm{I}}^{\mathrm{hr}}$ as a function of temperature, obtained from experimental data on Zircaloy-2. Note that, according to the experimental data, the threshold stress intensity factor for delayed hydride cracking at 570 K is about 9 MPa$\sqrt{\mathrm{m}}$. Experimental data on Zr–2.5Nb provide also relatively high values for the threshold stress intensity factor at elevated temperatures [22]; for example the threshold stress intensity factor for Zr–2.5Nb is about 10

MPa$\sqrt{\mathrm{m}}$ at 550 K. The experimental values of the threshold stress intensity factor include both the energy required for the generation of the new surface, due to crack growth, as well as any plastic dissipation in the zirconium alloy matrix, which surrounds the crack tip hydride. By taking $K_{\mathrm{I}}^{\mathrm{hr}}$ equal to the experimentally derived threshold stress intensity factor, the plastic dissipation near the crack tip has been also taken into account.

When crack growth is imminent or during crack growth, the material is damaged over a distance from the crack tip of the order the characteristic length, associated with the failure process. At the beginning of the damage zone, at the current crack tip, material is completely damaged and it cannot sustain significant traction. At the end of the damage zone, away from the crack tip, material damage initiates and therefore the maximum cohesive traction is sustained [24]. The zirconium alloy can sustain different maximum cohesive traction from that of the hydride. Therefore the maximum cohesive traction of the composite material along the crack plane depends on the hydride volume fraction. In the present analysis, the maximum cohesive traction is given by the following relation:

$$\sigma_{\max} = \sqrt{f\sigma_{\mathrm{hr}}^2 + (1-f)\sigma_{\mathrm{Zr}}^2}, \tag{29}$$

which is derived by assuming that the part of de-cohesion energy during loading satisfies a relation similar to (26). In (29), σ_{Zr} is the maximum cohesive traction, sustained by the material, when crack growth is imminent or during crack growth and when there is no hydride along the crack plane over a distance from the crack tip $X \gg \delta_0$. According to analytical and numerical studies for the crack tip field in elastic plastic materials (e.g. [28–30]), the maximum hoop stress, along the crack plane, is nearly equal to three times the yield stress of the material. Therefore, the maximum cohesive traction, σ_{Zr}, which is equal to the maximum hoop stress along the crack plane, when crack growth is imminent or during crack growth, is taken equal to three times the yield stress of the material. Note that, in the present study, the zirconium alloy has been assumed to be linear elastic in the bulk of the body. However, in deriving the de-cohesion constitutive relations, the elastic–plastic behavior of zirconium alloy has been considered. In other words, it has been assumed that plastic flow is limited in the de-cohesion layer.

In relation (29), σ_{hr} denotes the maximum cohesive traction, sustained by the material, when crack growth is imminent or during crack growth and when there is only hydride along the crack plane over a distance from the crack tip $X \gg \delta_0$. δ-hydride is a brittle phase. It is assumed that a brittle phase fractures, when a critical principal stress is applied, which is equal to the fracture strength of the phase. Consequently σ_{hr} is assumed to be equal to the hydride fracture strength. Shih and Puls [22] provide an estimate of hydride fracture strength which is considered to be proportional to Young's modulus of the material. Table 1 presents the value of hydride strength, obtained by using Shi–Puls relation, also used in [27].

Consider a particle of the de-cohesion layer ahead of a crack tip. Due to hydrogen diffusion and hydride formation, hydride volume fraction changes locally with time. Consequently the de-cohesion properties at the particle, under consideration, change with time. Maximum cohesive traction is reached, when δ_n corresponds to a normal traction, satisfying relation (29). As time increases, de-cohesion energy continues to change according to relation (26). Unloading starts, when relation (24) is satisfied. It is assumed that de-cohesion energy does not change during unloading.

The de-cohesion model is a mathematical/numerical tool for the simulation of damage and crack growth. It has been used for the simulation of delayed hydride cracking [16], which is a physical failure mechanism operating in zirconium alloys. In the present study, only the initial development of damage is considered. The simulation of delayed hydride cracking will be presented in a following paper.

3. Finite element implementation

The finite element implementation of the constitutive relations for the deformation and de-cohesion problem has been discussed in previous papers (e.g. [23,24]). The implementation is based on the principle of virtual work. In the following a short discussion is presented for the finite element implementation of the governing Eqs. (6) and (12) for hydrogen diffusion and non-mechanical energy flow, respectively.

The governing equations are supplemented by the following initial and boundary conditions:

$$C^{\mathrm{HT}} = C_0^{\mathrm{H}} \quad \text{at } t = 0, \tag{30}$$

$$T = T_0 \quad \text{at } t = 0, \tag{31}$$

$$C^{\mathrm{HT}} = C_{\mathrm{b}}^{\mathrm{H}} \quad \text{on } S_{\mathrm{b}}, \tag{32}$$

$$J_k^{\mathrm{H}} n_k = \varphi^{\mathrm{H}} \quad \text{on } S_{\varphi}. \tag{33}$$

$$T = T_s \quad \text{on } S_T, \tag{34}$$

$$-k\frac{\partial T}{\partial x_i} n_i = \varphi^{\mathrm{E}} \quad \text{on } S_F, \tag{35}$$

where C_0^{H} and T_0 are the initial hydrogen concentration and temperature which may vary within material volume V. If C_0^{H} is larger than the hydrogen terminal solid solubility, the initial hydrogen concentration in the solid solution equals the terminal solid solubility and the initial hydride volume fraction is calculated according to (7). A similar comment is valid for C_b^H which is the prescribed hydrogen concentration on S_b, a part of the bounding surface S. Note that, for the calculation of C^{TS}, stress and temperature distributions have to be taken into account. φ^H is the prescribed hydrogen flux on S_φ and T_s is the prescribed temperature on S_T. Also φ^E is the prescribed heat flux on S_F. Note that $S_b \cup S_\varphi = S$ and $S_T \cup S_F = S$. The quantities C_b^H, φ^H, T_s and φ^E may vary with time. The above general boundary conditions are specialized in order to approach the fuel cladding conditions which are encountered during the operation of the reactor [7].

The finite element equations are derived from variational descriptions of diffusion and energy flow. For this purpose variations of hydrogen concentration, δC^H, and temperature, δT, are considered, which satisfy the boundary conditions. Therefore:

$$\delta C^H = 0 \quad \text{on } S_b, \tag{36}$$

$$\delta T = 0 \quad \text{on } S_T. \tag{37}$$

Relation (6) is multiplied by a hydrogen concentration variation, satisfying (36). Subsequently it is integrated over the volume V. After some elaboration the following expression is derived, which is valid at any time t:

$$\begin{aligned} &\int_V \delta C^H \frac{dC^{HT}}{dt} dV \\ &= -\int_{S_\varphi} \delta C^H \varphi^H dS - \int_V (1-f) D^H \frac{\partial C^H}{\partial x_k} \frac{\partial(\delta C^H)}{\partial x_k} dV \\ &\quad - \int_V (1-f)\left(-\frac{D^H \overline{V}^H}{3RT} \frac{\partial \sigma_{mm}}{\partial x_k} + \frac{D^H Q^H}{RT^2} \frac{\partial T}{\partial x_k} \right) \\ &\quad \times C^H \frac{\partial(\delta C^H)}{\partial x_k} dV. \end{aligned} \tag{38}$$

Similarly, relation (12) is multiplied by a temperature variation, satisfying (37). Subsequently it is integrated over the volume V and the following expression is derived, which is valid at any time t:

$$\begin{aligned} &\int_V \delta T \, \rho c_p \frac{dT}{dt} dV + \int_V \delta T \, \frac{\Delta \overline{H}^{hr}}{\overline{V}^{hr}} \frac{df}{dt} dV \\ &= -\int_{S_F} \delta T \, \varphi^E dS - \int_V k \frac{\partial T}{\partial x_i} \frac{\partial(\delta T)}{\partial x_i} dV \\ &\quad - \int_V \delta T \, J_n^H \frac{\partial \mu^H}{\partial x_n} dV. \end{aligned} \tag{39}$$

Spatial discretization is obtained by introducing the usual finite element interpolation for hydrogen concentration, hydride volume fraction, temperature and displacement. Direct integration of Eqs. (38) and (39), as well as of the respective equations for material deformation and de-cohesion, is performed. For this purpose, time derivatives are calculated by considering linear hydrogen concentration, hydride volume fraction and temperature variations over a time interval Δt. Details are given in [31].

4. Simulation of Sawatzky's experiment

A Zircaloy-2 cylinder of 1.2 cm in diameter and 2.5 cm in length, with initial uniform hydrogen concentration 130 ppm by weight (= 837 mol/m^3) was subjected to a temperature difference of 347°C for 34 days [4]. Hot and cold end temperatures of 477°C and 130°C, respectively, were imposed by placing the specimen between a heated stainless steel cylinder and a water-cooled brass plate. Glass wool was wrapped around the specimen to reduce heat losses through the cylindrical surface of the specimen. Also any hydrogen losses were minimized by developing, before the experiment, an oxide surface layer which is impermeable to hydrogen.

The experiment was simulated by considering a cross-section containing the axis of the cylindrical specimen. The initial conditions were $C^{HT}(t=0) = 837$ mol/m^3 and $T(t=0) = 750 + (403 - 750)x_1/0.025$ K. In addition to the prescribed temperatures, given above, it was considered that the heat flux was zero at the rest of the boundary. Finally, the hydrogen flux was taken equal to zero everywhere at the boundary. The problem was solved by considering only energy flow and hydrogen diffusion. The development of compressive stresses, in the area of hydride formation was neglected, due to the small value of hydride volume fraction. The numerical results are presented in Fig. 1 together with the experimental data [4]. The agreement between finite element and experimental results is very good. Note that Marino has been also successfully simulated Sawatzky's experiment by using the same material properties [32].

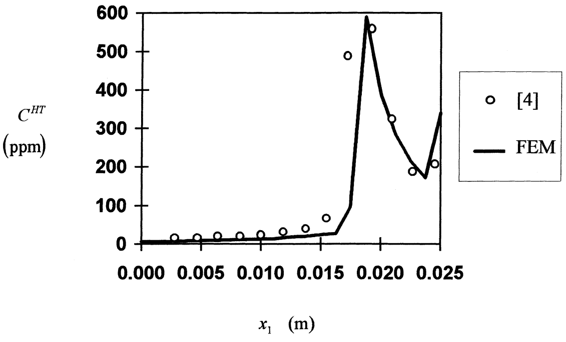

Fig. 1. Hydrogen distribution in a Zircaloy-2 cylinder, after a 34-day anneal under a temperature difference 130–477°C; experimental [4] and finite element results.

In Appendix A, a similar problem is considered for hydrogen concentration below terminal solid solubility; in this case, the finite element results are successfully compared with an exact analytical solution.

5. Hydride formation and damage ahead of a crack

5.1. Boundary value problem

The present boundary value problem has been designed in order to estimate the effect of surface cracks on initial hydride precipitation and damage in the cladding of light water reactor fuel rods. The most critical case corresponds to a crack along the rod axis. During reactor operation, the rod is subjected to external pressure by coolant water, internal pressure by helium gas and fission products, as well as to stresses, caused by fuel pellet-cladding mechanical interaction [33]. The combined effect may lead to the development of significant tensile hoop stresses. On the external rod surface, zirconium oxidation by coolant water leads to the generation of hydrogen, which subsequently diffuses in the cladding. The heat, which is generated in the fuel pellet, is transferred through the cladding to the water. The heat transfer process leads to the development of temperature gradients in the fuel cladding with significant effects on hydrogen distribution [7].

The development of external axial cracks has been observed in experiments, conducted by ABB Atom; fuel rods hydrided significantly, during service, have been used in ramp tests. Cracks can also develop on the inner side of a cladding tube, due to stress corrosion cracking caused by iodine and/or caesium, which are produced during nuclear fission. However, this mechanism is not under consideration.

In the present preliminary study, the geometry has been approximated by a cracked plate. Note that this approximation is good for small cracks and initial damage growth. In the present problem the crack length is less than 1/60 of the cladding tube inner radius [7]. Also the difference between the temperature distributions in the cladding cylinder, under consideration [7], and a plate of the same thickness, both subjected to the same surface temperatures, is negligible. The boundary value problem is shown in Fig. 2. The plate thickness, w, is taken to be equal to the actual cladding wall thickness (in this case $w = 0.8$ mm). A long planar surface crack of depth a $(= 0.1w)$ has been considered on one side. A remote tensile stress, σ_{ap}, is applied normal to the crack faces. The stress builds up gradually at a rate of 10 MPa/s, according to previous studies for pellet-cladding mechanical interaction [33]. The remote stress is considered to be constant after the maximum of 300 MPa is reached.

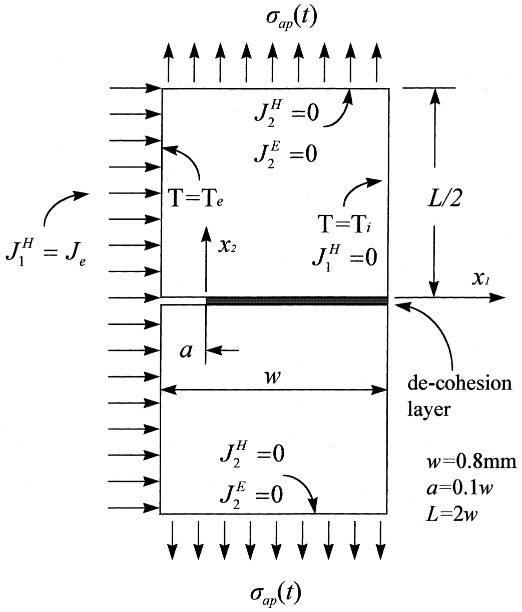

Fig. 2. Boundary value problem for the simulation of hydrogen embrittlement of a Zircaloy-2 cracked plate under tension and temperature gradient. Due to symmetry with respect to x_1-axis, only the upper half of the plate has been analyzed. When material damage is neglected, there is no de-cohesion layer, along the crack plane.

The oxidation process is assumed to produce a constant inflow of hydrogen on the crack-side surface of the plate, which is equal to 0.122×10^{-7} mol/(m^2 s) [7]. The same inflow of hydrogen is also assumed to occur on the crack faces. A zero hydrogen flux is considered on the other side of the plate, where stress and temperature gradients do not allow hydrogen outflow. Symmetry conditions require also zero hydrogen flux on the crack plane as well as on the remote plane, where σ_{ap} is applied. The initial hydrogen distribution is assumed to be uniform, equal to 2500 mol/m^3 $(= 388$ ppm$)$, which corresponds to 1900 days of reactor operation according to reference [7].

The temperature on both plate surfaces is constant, being equal to 567 K, on the crack side, and 607 K, on the other side. The initial temperature distribution is assumed to be linear across the thickness of the plate. The temperature distribution is in agreement with previous studies on hydrogen and temperature distribution in fuel cladding [7]. Symmetry conditions require that the heat flux is zero on the crack plane as well as on the remote plane, where σ_{ap} is applied.

Fig. 3(a) shows the finite element mesh for only half of the plate, needed to be analyzed. 1079 quadrilaterals, made of four cross triangles, have been used. On the triangular level, the first member of the triangular element family is considered, with three nodes at the ver-

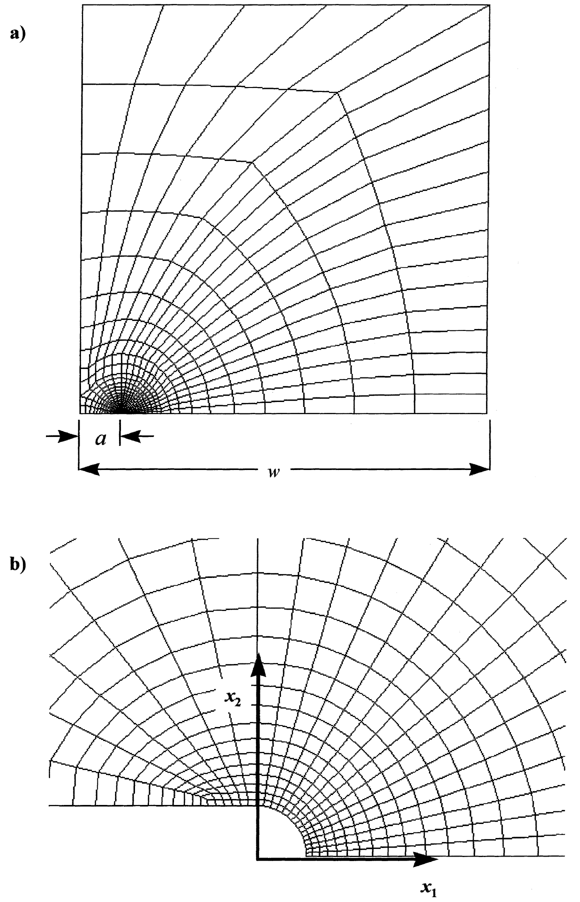

Fig. 3. Finite element mesh, used for the simulation of hydride formation and damage ahead of a crack: (a) upper half of the plate; (b) near-tip region.

tices. The near tip region of the finite element mesh and the coordinate system is shown in Fig. 3(b). The x_1-axis is normal to the crack front and lies on the crack plane. The crack has a circular profile at the tip with radius $r = 0.5$ μm. According to the boundary conditions, no variation of the field quantities occurs along the crack front and plane strain conditions prevail.

Numerical simulations have been performed for a period of 150 s. Two cases have been considered: (i) a perfect material without any damage ahead of the crack tip and (ii) damage growth ahead of the crack tip by using de-cohesion model.

6. Discussion

According to the discussion in Section 2, hydrogen redistribution is affected by concentration, stress and temperature gradients. Their combined effect on hydride precipitation near the crack tip is presented in Fig. 4, where the hydride volume fraction distribution along the crack line is shown as time progresses. The results in Fig. 4 were derived by neglecting material damage, ahead of the crack tip. Consequently, near tip stresses are larger than those which can be sustained by the material, leading to over-estimation of hydride volume fraction near the crack tip. This effect is clarified later on when the de-cohesion model results are presented. However, the expected hydrogen embrittlement mechanism is verified; hydrogen diffuses towards the crack tip, hydride precipitates and, if the remote loading is large enough, the hydride fractures and the crack advances. Indeed hydride volume fraction increases significantly, after a few seconds, as the crack tip is approached; note that the initial hydride volume fraction in the near-tip region, without any application of remote loading, is equal to 0.02.

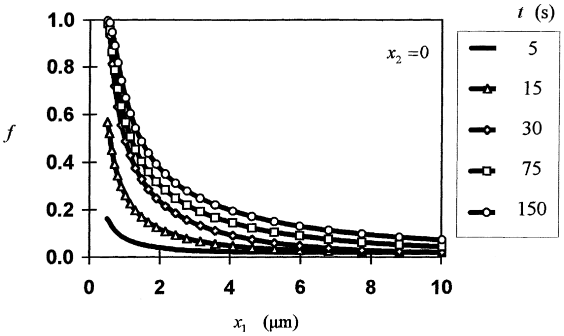

Fig. 4. Hydride volume fraction distribution along the crack line, as time progresses. No material damage has been considered.

The crack tip field plays a significant role on hydrogen embrittlement by affecting (i) hydrogen flux and (ii) hydrogen terminal solid solubility. Fig. 5 shows the distribution of the quantity$(\sigma_{kk}/\sigma_{\mathrm{ap}})\sqrt{x_1/a}$ along the crack line as time progresses, when material damage is neglected. Similar results have been also derived by using de-cohesion model. Note that the square root singularity dominates at distances larger than 25 μm which

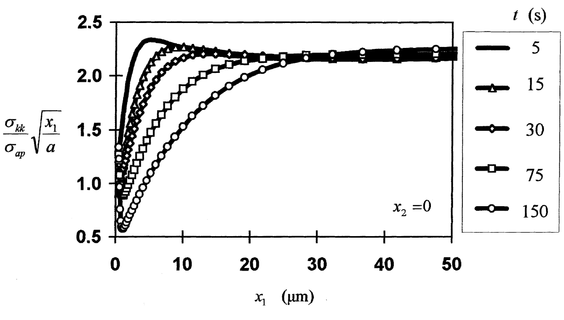

Fig. 5. Normalized stress trace distribution along the crack line, as time progresses.

is an order of magnitude larger than the expected hydride thickness. Indeed, according to the K-field distribution along the crack plane (see for example [26]), the stress trace is given by the following relation:

$$\sigma_{kk} = \frac{2(1+\nu)K_{\mathrm{I}}}{\sqrt{2\pi x_1}}, \tag{40}$$

where K_{I} is the stress intensity factor of the dominating mode-I K-field. Consequently the normalized stress trace, presented in Fig. 5, is constant within the annulus of K-field dominance

$$\frac{\sigma_{kk}}{\sigma_{ap}}\sqrt{\frac{x_1}{a}} = \frac{\sqrt{2}(1+\nu)K_{\mathrm{I}}}{\sigma_{ap}\sqrt{\pi a}} = \mathrm{const.} \tag{41}$$

Note that, according to Fig. 5, the normalized stress trace is nearly equal to 2.2 for $x_1 > 25$ μm. Therefore, one may calculate, by using relation (41), that the stress intensity factor of the dominating K-field is nearly equal to 5.5 $\mathrm{MPa}\sqrt{\mathrm{m}}$.

Near the crack tip, the stress trace deviates from the K-field distribution due to the expansion of the precipitated hydride and the development of compressive stresses, mainly perpendicularly to the (x_1, x_2) plane.

The effect of stress on hydrogen terminal solid solubility is shown in Fig. 6. The hydrogen concentration in the solid solution is presented along the crack line, as the time progresses. Note that, due to the presence of hydride, the hydrogen concentration is identical to the terminal solid solubility. As remote loading increases, for $t < 30$ s, near tip hydrostatic stress increases. Consequently, according to relation (15), the hydrogen terminal solid solubility decreases. For $t > 30$ s, the compressive stresses, which are associated with hydride precipitation, lead to the decrease of near tip hydrostatic stress. For this reason the hydrogen terminal solid solubility increases near the crack tip for $t > 30$ s, affecting hydride precipitation.

The contribution of stress, temperature and concentration gradients on total hydrogen flux towards the crack tip is presented in Fig. 7, for $t = 5$ s. All the terms direct hydrogen towards the crack tip. The stress gradient has a dominant contribution over distances of the order of hydride thickness. However, at a distance away from the crack tip, which is an order of magnitude larger than hydride thickness (i.e. at a distance larger than 20 μm) the effect of temperature gradient becomes more important. Note that, due to the energy flow boundary conditions and the geometry, the temperature gradient is nearly constant leading to a slightly changing hydrogen flux contribution everywhere in the fuel cladding. The temperature gradient contribution decreases significantly only in the near tip region, due to the precipitation of hydride. It is also interesting to mention, that the concentration gradient effect on hydrogen flux increases as the crack tip is approached. This trend is attributed to the decrease of the hydrogen terminal solid solubility, which is caused by the stress field, shown in Fig. 6. Both Figs. 6 and 7 show the strong effects of stress on hydrogen diffusion and terminal solid solubility. Consequently, they show the importance of introducing the stress terms in relations (13) and (15) for hydrogen chemical potential and terminal solid solubility, respectively.

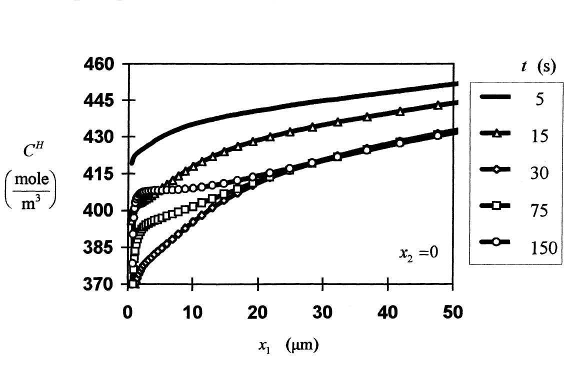

Fig. 6. Distribution of hydrogen concentration in solid solution along the crack line, as time progresses.

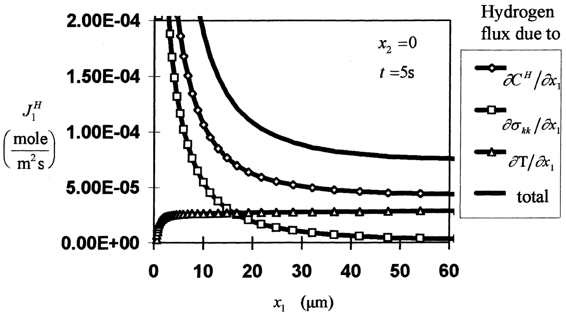

Fig. 7. Hydrogen flux distribution along the crack line. The contributions of hydrogen concentration, stress and temperature gradients are presented separately. All fluxes are directed towards the crack tip.

The effect of near tip material damage on hydrogen redistribution is taken into account by considering decohesion model. The finite element calculations are repeated by using the hydrogen embrittlement model coupled with the de-cohesion model. Near tip damage growth is shown in Fig. 8, where L_{D} is the damage zone size along the crack plane, being equal to the maximum distance from the crack tip, over which cohesive traction has reached the maximum value, sustained by the material

$$L_{\mathrm{D}} = \max\{x_1(\sigma_{22} = \sigma_{\max}) - r\}. \tag{42}$$

Material damage includes Zircaloy-2 yielding and possibly local fracture of hydride platelets, within the decohesion layer. The damage growth, produced by the application of the remote loading of 300 MPa, is not

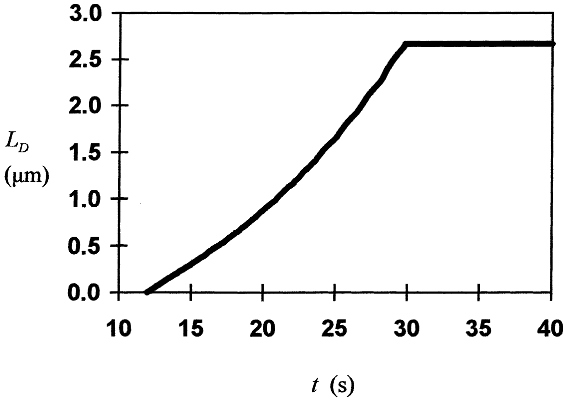

Fig. 8. Damage growth ahead of the crack tip.

associated with complete material failure at or near the crack tip. Indeed, according to the material properties, presented in Table 1, the threshold stress intensity factor of Zircaloy-2 for delayed hydride cracking, $K_{\mathrm{I}}^{\mathrm{hr}}$, is about equal to 9 MPa$\sqrt{\mathrm{m}}$ at 570 K. This value is larger than the stress intensity factor of the dominating K-field, according to the previous discussion.

Material damage limits the stress level near the crack tip and consequently reduces hydrogen flux and accumulation. The hydride volume fraction distribution along the crack line, derived by using de-cohesion model, is presented in Fig. 9, for the same time intervals as in Fig. 4. Indeed, according to Figs. 9 and 4, material damage results into significantly smaller hydride volume fraction near the crack tip. Fig. 9 also shows that, by introducing material damage, the numerical simulation predicts hydride precipitation at some distance from the crack tip. Thus, a thin ligament develops between the crack tip and the near tip hydride. The hydride volume fraction is relatively small in this ligament. In recent delayed hydride cracking simulations [16], a hydride of length about equal to 10 μm fully develops (i.e. $f > 0.9$) at some distance, of the order of μm, from the crack tip. Subsequently the hydride fractures and leaves behind a ligament, which is stretched plastically. Note that the mechanism of crack growth by hydride formation and fracture, which leaves behind intact ligaments, has been observed in delayed hydride cracking experiments for Zr–2.5Nb alloy [34].

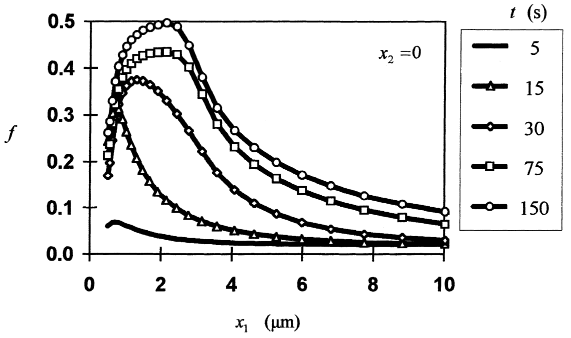

Fig. 9. Hydride volume fraction distribution along the crack line, as time progresses. Material damage has been taken into account by de-cohesion model.

7. Conclusions

A robust mathematical model for the hydrogen embrittlement of zirconium alloys has been developed. The model takes into account the coupling of the operating physical processes, namely: (i) hydrogen diffusion, (ii) hydride precipitation, (iii) non-mechanical energy flow and (iv) hydride/solid-solution deformation. Material damage, is also simulated by using de-cohesion model, which takes into account the time variation of energy of de-cohesion and maximum cohesive traction, due to the time-dependent hydride precipitation.

The hydrogen embrittlement model has been implemented numerically into a finite element framework. It has been also tested successfully against Sawatzky's experiment and exact analytical solutions on hydrogen diffusion and hydride precipitation under temperature gradient.

Based on this model, results on hydrogen embrittlement initiation of a Zircaloy-2 cracked plate, under tensile stress and temperature gradient, are given. The initial and boundary conditions approach those encountered in the fuel cladding of light water reactors, during operation. According to the numerical results, the contribution of stress gradient on hydrogen flux becomes dominant near the crack tip. This effect is attributed to the dependence of the hydrogen chemical potential and terminal solid solubility on hydrostatic stress. On the other hand, thermal transport is more important away from the crack tip. The problem is also studied by considering near-tip material damage, which has significant implications on the prediction of hydride precipitation. Material damage results into significantly smaller hydride volume fraction near the crack tip.

Acknowledgements

A.G.V. acknowledges the support of ABB Atom AB under the contracts 4500026874 and 4500028097.

Appendix A. One-dimensional hydrogen diffusion in solid solution under constant temperature gradient

The following one-dimensional problem of hydrogen thermal transport has been solved analytically in order to check the performance of the finite element code with respect to hydrogen diffusion. A Zircaloy-2 cylinder of length L is considered with an initially uniform hydrogen concentration. The cylinder is imposed on a linear temperature distribution, along the axis, and the hydrogen concentration is examined, after the elapse of sufficient time and the development of steady-state conditions. No stress is applied on the cylinder. The initial and boundary conditions are designed in order to produce hydrogen concentration variations only along the axis of the cylinder. Consequently a one-dimensional problem is derived, with the following initial:

$$C^{\mathrm{HT}}(t=0) = C_0 = \text{const.}, \quad 0 \leqslant x_1 \leqslant L, \tag{A.1}$$

and boundary conditions:

$$\int_0^L C^{\mathrm{HT}}(x_1,t)\mathrm{d}x_1 = C_0 L = \text{const.}, \quad t \geqslant 0. \tag{A.2}$$

x_1 is the axis of the cylinder and C^{HT} is the total hydrogen concentration. In the present problem, the initial hydrogen concentration is below the terminal solid solubility everywhere in the cylinder. Consequently, hydrogen is in solid solution and $C^{\mathrm{HT}} = C^{\mathrm{H}}$. Note that the boundary condition corresponds to zero hydrogen losses, through the surface of the cylinder. In an experiment, this condition corresponds to the development of a zirconium oxide layer on the specimen surface, which is relatively impermeable to hydrogen.

The absolute temperature distribution is given by the following relation:

$$T(x_1,t) = T_0 + (T_L - T_0)\frac{x_1}{L}, \quad 0 \leqslant x_1 \leqslant L, \ t \geqslant 0. \tag{A.3}$$

T_0 and T_L are the temperatures at the ends of the cylinder.

At steady-state, hydrogen flux is zero. Consequently, hydrogen distribution is governed by the following differential equation:

$$J_1^{\mathrm{H}} = -D^{\mathrm{H}}\frac{\mathrm{d}C^{\mathrm{H}}}{\mathrm{d}x_1} - \frac{D^{\mathrm{H}}C^{\mathrm{H}}Q^{\mathrm{H}}}{RT^2}\frac{\mathrm{d}T}{\mathrm{d}x_1} = 0, \tag{A.4}$$

which is easily integrated to provide the following general solution:

$$C^{\mathrm{H}}(x_1) = A\exp\left(\frac{Q^{\mathrm{H}}}{RT}\right). \tag{A.5}$$

A is an integration constant, which depends on the boundary conditions:

$$A = C_0(T_L - T_0)\left(\int_{T_0}^{T_L} \exp\left(\frac{Q^{\mathrm{H}}}{RT}\right)\mathrm{d}T\right)^{-1}. \tag{A.6}$$

The integration in relation (A.6) provides

$$\begin{aligned}\int_{T_0}^{T_L} & \exp\left(\frac{Q^{\mathrm{H}}}{RT}\right)\mathrm{d}T \\ &= \left[T_L\exp\left(\frac{Q^{\mathrm{H}}}{RT_L}\right) - T_0\exp\left(\frac{Q^{\mathrm{H}}}{RT_0}\right)\right] \\ &\quad - \frac{Q^{\mathrm{H}}}{R}\left[\mathrm{Ei}\left(\frac{Q^{\mathrm{H}}}{RT_L}\right) - \mathrm{Ei}\left(\frac{Q^{\mathrm{H}}}{RT_0}\right)\right],\end{aligned} \tag{A.7}$$

where Ei(x) is the exponential integral function [35].

Calculations have been performed for

$$C_0 = 60 \text{ ppm} = 386.3095 \text{ mol/m}^3,$$
$$T_0 = 773 \text{ K} \quad \text{and} \quad T_L = 573 \text{ K}.$$

$L = 0.025$ m and the material properties are presented in Table 1. The finite element mesh, which has been also used in the simulation of Sawatzky's experiment, is an orthogonal 0.025×0.012 m^2, which is divided in 20×10 equal size parallelograms.

The finite element results, when steady state is reached, are compared with the analytical solution in Fig. 10. The error, defined as the maximum discrepancy of the finite element results from the analytical solution, is 0.027%. Note that the final hydrogen concentration is below terminal solid solubility. Consequently the above analysis is valid.

The calculations have been performed, by considering that hydrogen terminal solid solubility in Zircaloy-2 is given by the relation, $C^{\mathrm{TS}} = 2 \times 10^5 \exp(-25\,150/RT)$ (mol/m^3). This relation has been taken from Table 1 of Ref. [21] and corresponds to dilatometry-cooling measurements of Slattery [36]. According to the above relation, the terminal solid solubility of hydrogen at 573 K is 1019.24 mol/m^3. Note that the hydrogen terminal solid solubility has been only used for verifying that

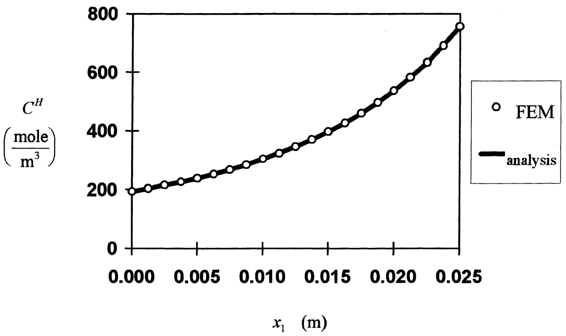

Fig. 10. Steady-state hydrogen concentration distribution in a Zircaloy-2 cylinder, subjected to a constant temperature gradient, derived by mathematical analysis and finite element calculations. Hydrogen is in solid solution. No hydrogen losses were allowed through the specimen surface, before reaching steady-state conditions.

hydrogen is in solid solution and it does not influence the above calculations.

The numerical model has been also compared successfully with the following analytical solutions: (i) One-dimensional hydrogen diffusion in solid solution under constant stress and temperature gradients; the error between the numerical and the exact analytical solution is 0.002%. (ii) One-dimensional hydrogen diffusion and hydride formation under constant temperature gradient; the error between the numerical solution and the approximate analytical solution of Sawatzky [4] is 0.029%. These problems are discussed in detail in [37].

References

[1] P.G. Shewmon, Diffusion in Solids, McGraw-Hill, New York, 1963.
[2] C.E. Coleman, D. Hardie, J. Less-Common. Met. 11 (1966) 168.
[3] F. Garzarolli, R. Holzer, Nucl. Energy 31 (1992) 65.
[4] A. Sawatzky, J. Nucl. Mater. 2 (1960) 321.
[5] J.M. Markowitz, Trans. Metall. Soc. AIME 221 (1961) 819.
[6] R.C. Asher, F.W. Trowse, J. Nucl. Mater. 35 (1970) 115.
[7] K. Forsberg, A.R. Massih, J. Nucl. Mater. 172 (1990) 130.
[8] B.F. Kammenzid, D.G. Franklin, H.R. Peters, W.J. Duffin, in: E.R. Bradley, G.P. Sabol (Eds.), Zirconium in the Nuclear Industry, 11th International Symposium, ASTM STP 1295, American Society for Testing of Materials, 1996, p. 338.
[9] C.E. Ells, C.J. Simpson, in: I.M. Bernstein, A.W. Thompson (Eds.), Hydrogen in Metals, ASM, Metals Park, 1974, p. 345.
[10] H. Maki, M. Sato, J. Nucl. Sci. Technol. 12 (1975) 637.
[11] J. Lufrano, P. Sofronis, H.K. Birnbaum, J. Mech. Phys. Solids 44 (1996) 179.
[12] K.G. Denbigh, The Thermodynamics of the Steady State, Methuen, London, 1951.
[13] A. Needleman, J. Appl. Mech. 54 (1987) 525.
[14] A.G. Varias, N.P. O'Dowd, R.J. Asaro, C.F. Shih, Mater. Sci. Eng. A 126 (1990) 65.
[15] V. Tvergaard, J.W. Hutchinson, J. Mech. Phys. Solids 40 (1992) 1377.
[16] A.G. Varias, Simulation of hydride formation and fracture in LWR fuel cladding – Crack growth under constant temperature, Solid Mechanics Research Office, PR-06-09-99, 1999.
[17] A.G. Varias, Mathematical Model for Hydrogen Diffusion, Energy Flow and Hydride Formation in Zirconium under Stress, Solid Mechanics Research Office, BR-04-10-98, 1998.
[18] C. Truesdell, R. Toupin, in: S. Flügge (Ed.), Encyclopedia of Physics, Springer, Berlin, vol. 3/1, 1960, p. 226.
[19] J.C.M. Li, R.A. Oriani, L.S. Darken, Zeitschrift fur Physikalische Chemie NF 49 (1966) 271.
[20] J.D. Eshelby, Proc. Roy. Soc. London A 241 (1957) 376.
[21] M.P. Puls, Acta Metall. 29 (1981) 1961.
[22] S.-Q. Shi, M.P. Puls, J. Nucl. Mater. 208 (1994) 232.
[23] A.G. Varias, Comput. Mech. 21 (1998) 316.
[24] A.G. Varias, A.R. Massih, Temperature and constraint effects on hydride fracture in zirconium alloys, Eng. Fract. Mech., in press.
[25] J.R. Rice, in: H. Liebowitz (Ed.), Fracture: An Advanced Treatise, vol. II, Academic Press, New York, 1968, p. 191.
[26] M.F. Kanninen, C.H. Popelar, Advanced Fracture Mechanics, Oxford University, New York, 1985.
[27] D. Wäppling, A.R. Massih, P. Ståhle, J. Nucl. Mater. 249 (1998) 231.
[28] J.W. Hutchinson, J. Mech. Phys. Solids 16 (1968) 337.
[29] J.R. Rice, M. A. Johnson, in: M.F. Kanninen, W.F. Adler, A.R. Rosenfield, R.I. Jaffee (Eds.), Inelastic Behavior of Solids, McGraw-Hill, New York, 1970, p. 641.
[30] W.J. Drugan, J.R. Rice, T.-L. Sham, J. Mech. Phys. Solids 30 (1982) 447.
[31] A.G. Varias, Simulation of Hydride Formation and Fracture in LWR Fuel Cladding – Finite Element Model, Solid Mechanics Research Office, BR-05-11-98, 1998.
[32] G.P. Marino, Nucl. Sci. Eng. 49 (1972) 93.
[33] A.R. Massih, T. Rajala, L.O. Jernkvist, Nucl. Eng. Design 156 (1995) 383.
[34] L.A. Simpson, K. Nuttall, in: A.L. Lowe Jr., G.W. Parry (Eds.), Zirconium in the Nuclear Industry, ASTM STP 633, American Society for Testing and Materials, 1977, p. 608.
[35] M. Abramowitz, I.A. Stegun, Handbook of Mathematical Functions, Dover, New York, 1970.
[36] G.F. Slattery, J. Inst. Met. 95 (1967) 43.
[37] A.G. Varias, Simulation of hydride formation and fracture in LWR fuel cladding – Tests of the finite element code (Task 2), Solid Mechanics Research Office, BR-04-04-99, 1999.
[38] F.H. Huang, J. Nucl. Mater. 207 (1993) 103.
[39] J.J. Kearns, J. Nucl. Mater. 22 (1967) 292.
[40] R. Dutton, K. Nuttall, M.P. Puls, L.A. Simpson, Metall. Trans. A 8A (1977) 1553.
[41] M.P. Puls, Acta Metall. 32 (1984) 1259.
[42] D. L. Hagrman, G. A. Reymann, and R. E Mason (Eds.), MATPRO version 11, A Handbook of Materials Properties for Use in the Analysis of Light Water Reactor Fuel Rod Behavior, NUREG/CR-0479, TREE-1280, Rev 2, Department of Energy Publication.